CMES, vol.4, no.6, pp.707-718, 2003

Computational Simulation of Localized Damage by Finite Element Remeshing based on Bubble Packing Method

Soon Wan Chung[1], **Yoo Jin Choi**[1] **and Seung Jo Kim**[1]

Abstract: In this paper, an automatic finite element remeshing algorithm based on the bubble packing method is utilized for the purpose of numerical simulations of localized damage, because fine meshes are needed to represent the gradually concentrated damage. The bubble packing method introduces two parameters that easily control the remeshing criterion and the new mesh size. The refined area is determined by *a posteriori* error estimation utilizing the value obtained from Superconvergent Patch Recovery. The isotropic ductile damage theory, founded on continuum damage mechanics, is used for this damage analysis. It was successfully shown in the numerical examples (upsetting and extrusion problems) that the remeshing algorithm generates fine and regular meshes for the regions with distorted meshes and that the damage is localized in the refined zone.

keyword: Bubble packing method, Remeshing, Continuum damage mechanics, localization, metal forming.

Nomenclature:

$\boldsymbol{F}$:deformation gradient tensor
$\boldsymbol{R}$:rotation tensor
$\boldsymbol{U}$:right stretch tensor
$\boldsymbol{D}$:rate-of-deformation tensor
$\dot{\boldsymbol{E}}$, $\dot{\boldsymbol{P}}$:elastic and plastic strain rates
$\boldsymbol{S}$:rotation free stress or Dienes stress
ϕ :free energy potential
ψ :dissipative potential
d :isotropic damage variable
B :damage strain energy density release rate
z :internal variable denoting hardening behavior
h :hardness variable
ε^* :equivalent strain recovered by SPR
$\hat{\varepsilon}$:equivalent strain calculated by FEM
η^* :predicted relative error
$\eta^*_{\max}$:maximum permissible relative error
$\|e_\varepsilon\|$: L_2norm of strain error
$\|e_\varepsilon\|_{i,\max}$:maximum permissible error in i-th element
r_{ave} :average of radii of three vertexes(bubbles) in candidate element for refinement
r_{new} :radius of bubble belonging to a refining circle
q :control factor for r_{new}

1 Introduction

As the distorted meshes increase due to large deformations, the approximation error in the nonlinear problems also increases. Therefore, the adaptive refinement technique was implemented to prevent any difficulties in convergence. This technique distributes the refined meshes around a singular point, for *h*-refinement in elastic analysis [Zienkiewicz and Zhu(1987)], and substitutes regular meshes for the distorted meshes in large deformation problems, such as metal forming.[Khoei and Lewis(1999), PavanaChand and KrishnaKumar (1998), Yang and Heinstein and Shih(1989)]Also, refined meshes are generated for shear bands, which are narrow regions of intense plastic deformation[Ortiz and Quigley(1991), Batra and Ko(1992)] and the crack propagation direction is predicted by placing many fine meshes near the crack tip. [Potyondy and Wawrzynek and Ingraffea(1995), Tradegard and Nilsson and Ostlund(1998)]

The conventional adaptive mesh refinement consists of three parts: the remeshing criterion, the automatic mesh generation algorithm, and the transfer of state variables between the old and new meshes. The remeshing criterion generally is the *a posteriori* error estimation [Cheng(1998), Paulino and Menezes and Neto and

---

[1] Department of Aerospace Engineering, Seoul National University, San 56-1, Shinlim-dong, Kwanak-ku, Seoul, 151-742, Korea.

Martha(1999)], based on the error norm of strain (or stress), or the geometric distortion of elements. [PavanaChand and KrishnaKumar (1998)] The automatic mesh generation algorithm consists of the node connection method [Shimada and Gossard(1998), Lee and Hobbs(1999)], which distributes and connects the nodes, and the recursive domain decomposition method [Petersen and Rodrigues and Martins(2000)], which divides the computational domain until the desired mesh size is attained. The state variables computed at the integration point are usually transferred from the old mesh to the new mesh in three steps (old mesh Gauss point→old mesh node→new mesh node→new mesh Gauss point).

In this study, the adaptive remeshing technique is applied to ductile damage analysis. Ductile damage grows on a largely deformed region, concentrates gradually and finally develops into crack formations. Not only can the adaptive refinement diminish the error caused by the distorted element but it can also show the damage localization using the refined meshes.[Var and Owen (2001), Svedberg and Runesson(2000), Min and Tworzydlo and Xiques(1995)] The developed finite element code, for damage analysis, includes geometric nonlinearity, material nonlinearity and contact constraint with friction conditions. Also, the isotropic damage rule based on the theory of materials of type N [Kim and Kim and Kim(1995)] was adopted to describe the damage process of ductile material with large elasto-viscoplastic deformations. An automatic mesh generation and remeshing algorithm, based on the bubble packing method [Chung and Kim(2002)], was developed to generate linear triangular elements. This algorithm can easily control the remeshing criterion and new mesh size through two parameters, maximum permissible relative error and control factor for refined mesh. The axisymmetric upsetting process and the extrusion under plane strain condition were chosen as numerical experiments to show the capabilities of the adaptive remeshing algorithm in simulating damage localization.

2 Isotropic Ductile Damage Theory

The damage theory in this study is based on continuum damage mechanics (CDM). CDM (Lemaitre(1996), Hatzigeorgiou and Beskos(2002)) can be separated into two categories by the definition of the damage variable: the isotropic damage theory and the anisotropic damage theory. CDM can be applied to the following material properties by the range of application: ductility of metal, brittleness of concrete, fatigue and creep, etc. Recently, the damage localization by CDM has been investigated through many approaches such as a nonlocal model, a gradient model (Peerlings and Borst and Brekelmans and Geers(2002)) and a combined damage/plasticity model without nonlocal terms(Chen and Hu and Chen(2000)). This study utilized the isotropic damage theory for the application of ductile materials, and the theory is composed of kinematics and elasto-viscoplastic material rule. The contact constraint in the boundaries was implemented using the extended interior penalty method. [Kim and Kim(1993)]

2.1 Kinematics

According to the polar decomposition theorem, a right stretch tensor, $\boldsymbol{U}$, and a rotation tensor, $\boldsymbol{R}$, are obtained from a gradient deformation tensor $\boldsymbol{F}$(eq. (1)). Considering the deformation in the current rotation free configuration, the right stretch tensor is additively decomposed into the elastic and plastic parts (eq. (2)) [Kim and Chung(1998)].

$$\boldsymbol{F}=\boldsymbol{R}\boldsymbol{U} \tag{1}$$

$$\boldsymbol{U}=\boldsymbol{U}^e+\boldsymbol{U}^p-\boldsymbol{I} \tag{2}$$

Using eq. (1) and (2), a rate-of-deformation tensor, $\boldsymbol{D}$, is derived into eq. (3) where $\dot{\boldsymbol{U}}^e\boldsymbol{U}^{-1}|_{sym}$ and $\dot{\boldsymbol{U}}^p\boldsymbol{U}^{-1}|_{sym}$ are the elastic and plastic strain rate terms respectively.

$$\boldsymbol{D}=\boldsymbol{L}_{sym}=\boldsymbol{R}(\dot{\boldsymbol{U}}^e\boldsymbol{U}^{-1}|_{sym}+\dot{\boldsymbol{U}}^p\boldsymbol{U}^{-1}|_{sym})\boldsymbol{R}^t \tag{3}$$

$$\boldsymbol{R}^t\boldsymbol{D}\boldsymbol{R}=\dot{\boldsymbol{E}}+\dot{\boldsymbol{P}} \tag{4}$$

The conjugate objective stress of elastic strain or the rotation free stress, $\boldsymbol{S}$, is calculated by transforming the Cauchy stress, $\boldsymbol{\sigma}$, using the rotation tensor.

$$\boldsymbol{S}=\boldsymbol{R}^t\boldsymbol{\sigma}\boldsymbol{R} \tag{5}$$

2.2 Elasto-viscoplastic damage model

The elasto-viscoplastic rule is based on the theory of materials of type N, which consists of field equations and the following two potentials.

1) Free energy potential

$$\phi=\frac{1}{\rho_0}\left\{\frac{1-d}{2}\left[\lambda(tr\mathbf{E})^2+2\mu(tr\mathbf{E}^2)\right]\right.$$
$$\left.-h_1z-\frac{1}{m}(h_1-h_0)\mathbf{exp}(-mz)\right\}$$

2) Dissipative potential

$$\psi = D_0 \sum_{i=0}^{\infty} (-1)^{i+1} \frac{\beta^i h^{2i-1}}{i!(2i-1)\overline{J}_2^{\,i-0.5}} + \frac{1}{2} C_1 B^2 \mathbf{exp}\left[\left(\frac{1}{1-d}\right)^k\right] M(tr\,\mathbf{S})$$

where

$$\overline{J}_2 = \frac{1}{2} tr\left\{\overline{\mathbf{S}}' : \overline{\mathbf{S}}'\right\} \quad , \quad \overline{\mathbf{S}}' = \frac{\mathbf{S}'}{1-d} \quad ,$$

$$M(tr\,\mathbf{S}) = \begin{cases} 1 & if\ tr\,\mathbf{S} > 0 \\ 0.2 & if\ tr\,\mathbf{S} < 0 \end{cases}$$

Here, d and z are internal state variables which denote damage state and hardening behavior respectively. And B and h are the conjugate thermodynamic forces corresponding to d and z. The variable B corresponds to the strain energy density release rate in Lemaitre's isotropic damage model.[Lemaitre(1996)] The material constants (C_1,k) related with damage are determined by a simple tension test; the material used in this research is Al 2024 and its material constants are shown in Tab. 1 [Kim and Kim(1994)]. The final constitutive equations derived from differentiating the potentials are

$$\mathbf{S} = \frac{\rho}{\rho_0}(1-d)\left[\lambda(tr\mathbf{E})I + 2\mu\mathbf{E})\right], \tag{6}$$

$$B = -\frac{\rho}{2\rho_0}\left[\lambda(tr\mathbf{E})^2 + 2\mu(tr\mathbf{E}^2)\right], \tag{7}$$

$$h = \frac{\rho}{\rho_0}\left[h_1 + (h_0 - h_1)\mathbf{exp}(-mz)\right], \tag{8}$$

$$\dot{\mathbf{P}} = D_0 \frac{1}{2h\sqrt{\overline{J}_2}} \mathbf{exp}\left(-\frac{\beta h^2}{\overline{J}_2}\right)\overline{\mathbf{S}}', \tag{9}$$

$$\dot{d} = -C_1 B\,\mathbf{exp}\left[\left(\frac{1}{1-d}\right)^k\right] M(tr\,\mathbf{S}), \tag{10}$$

$$\dot{z} = \frac{1}{h}\overline{\mathbf{S}}' : \dot{\mathbf{P}}. \tag{11}$$

Table 1 : Mechanical properties and material constants of Al2024

Material constant	Symbol	Value
Young's modulus	E	72.4 GPa
Poisson's ratio	ν	0.32
Yield strength	Y	393 MPa
Initial damage threshold	D_0	1.35×10^7 $MPa/\mathbf{sec}$
Hardening constant	m	25
Initial hardness constant	h_0	1150 MPa
Ultimate hardness constant	h_1	1670 MPa
Damage magnification factor	C_1	1.27×10^{-7} $mm^2/(N\cdot\mathbf{sec})$
Damage slope factor	k	2.7

3 Adaptive Refinement Algorithm

In order to perform the adaptive refinement procedure for nonlinear Finite Element Analysis, additional algorithms, such as error estimation, refinement criterion, automatic mesh generation and transfer of state variables, were added (Fig. 1).

3.1 Automatic mesh generation

We utilized an automatic mesh generation algorithm based the on bubble packing method (BPM), which we had developed in a previous study [Chung and Kim(2002)]. The BPM determines the optimal nodal placements by finding the equilibrium positions using the attractive/repulsive interbubble forces. BPM considers the center of the bubble as the node and yields the nodal positions compatible with the given bubble size function. This method consists of the following steps.

(1^{st} step) Packing of bubbles on the boundary line

After the information on bubble size and boundary such as nodes, lines, etc. is read in the input data (Fig. 2(a)), the bubbles are packed along the boundary lines connecting nodes. (Fig. 2(b))

(2^{nd} step) Packing of bubbles on the surface

The bubbles are packed along the lines between the center of domain given in the input data and the vertexes.

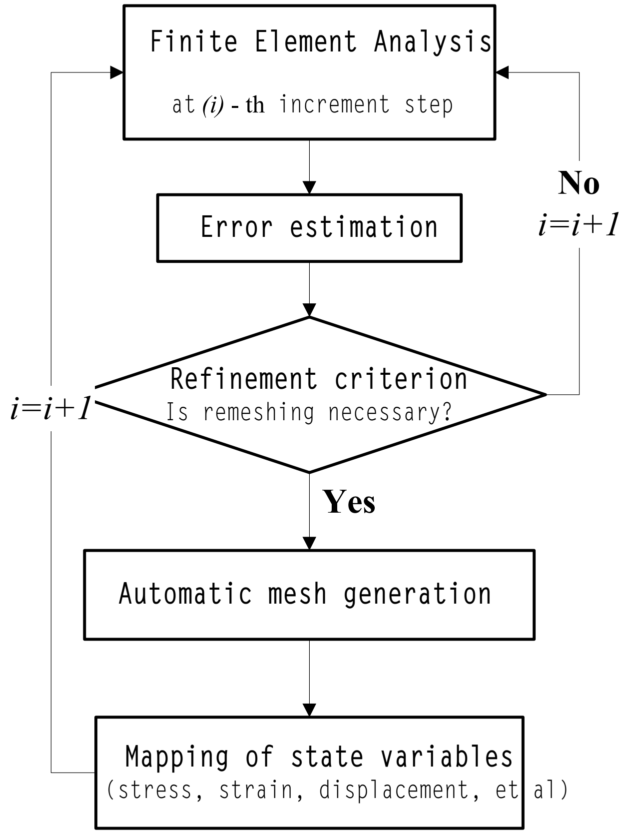

Figure 1 : Flowchart of remeshing algorithm

Then, bubbles are inserted in between two nodes on those different lines.(Fig. 2(c)) The nodes generated in a hollow domain such as a void are removed by the vertical ray shooting algorithm [Mulmuley(1994)]. (Fig. 2(d))

(3rd step) Physically based dynamic simulations

To get rid of gaps or overlaps between bubbles in the initial bubble placement, the bubble configuration balanced with interbubble attractive/repulsive forces is found. (Fig. 2(e)) The forces [Shimada and Gossard(1998)] applied at boundary bubbles are projected to the boundary line to constrain bubbles on the boundary. Also, the following equation of motion of the i-th bubble is integrated by the fourth-order Runge Kutta method.

$$m_i\ddot{x}_i + c_i x_i = f_i \tag{12}$$

Next, triangular meshes are generated beginning at the boundary using the Delaunay triangulation with advancing front concept [Du(1998)]. The recursive/adaptive bubble population controls were used to obtain larger amounts of regular triangle meshes. As the node numbers produced by automatic mesh generation are distributed randomly, the bandwidth minimization technique [Chung and Kim(2002)] is also incorporated for the band solver, which is used to solve the resulting simultaneous linear equations. Since nodal placement and connection in this algorithm starts at the boundary lines, accurate updates of boundary information are important while the boundary nodes are being added. A flowchart of a series of algorithms is shown in Fig. 3.

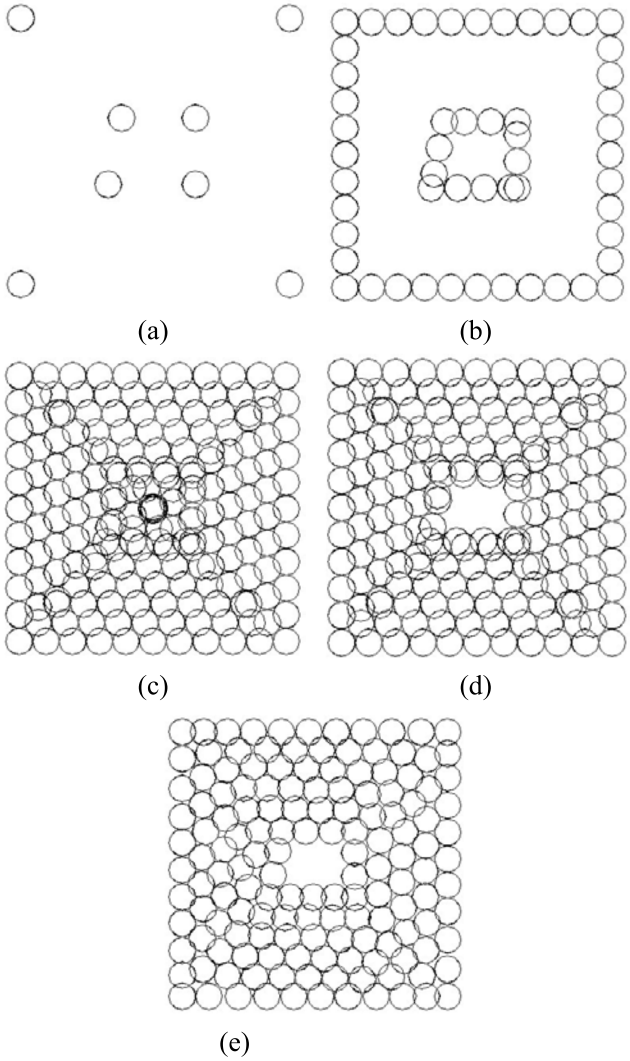

Figure 2 : Procedure of node distribution based on bubble packing method ((a) Nodes given in input data, (b) Boundary line bubble packing, (c) Surface bubble packing-1, (d) Surface bubble packing-2, (e) Bubble distribution after dynamic simulation)

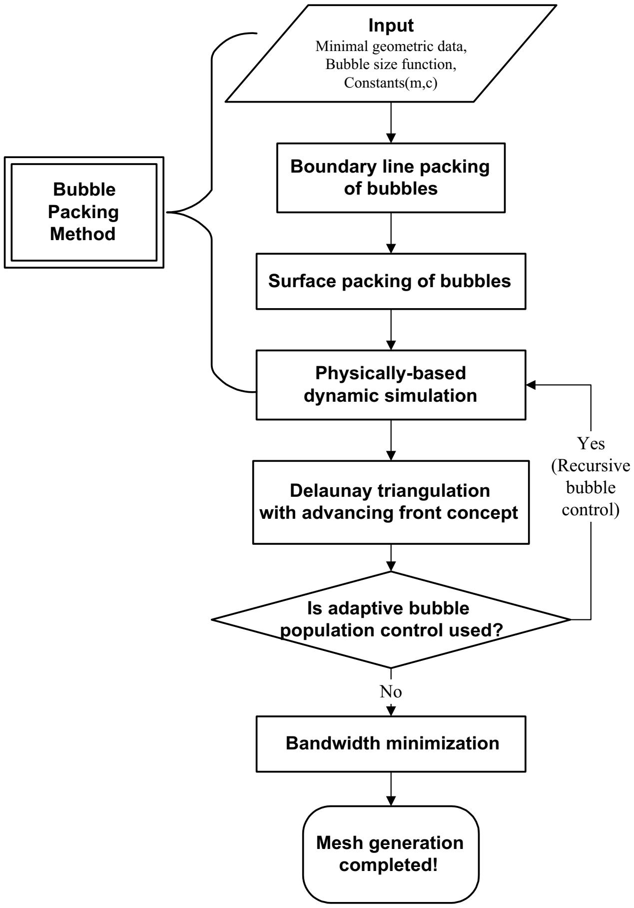

Figure 3 : Flowchart of automatic mesh generation

3.2 Error estimation and Refinement criterion

Generally, refined meshes are generated around elements with large errors. Therefore, *a posteriori* error calculation using the equivalent strain was utilized in this study. The strain error using the recovered value is defined as

$$e_\varepsilon \equiv \varepsilon^* - \hat{\varepsilon}. \tag{13}$$

Here, ε^* is the recovered strain value obtained through Superconvergent Patch Recovery (SPR) [Zienkiewicz and Zhu(1992)] and $\hat{\varepsilon}$ is the finite element solution. The L_2 norm of strain error and a predicted relative error η^* can be written as

$$\|e_\varepsilon\| = \sqrt{\sum_{i=1}^{m} \|e_\varepsilon\|_i^2} = \sqrt{\sum_{i=1}^{m} \int_{\Omega_i} (\varepsilon^* - \hat{\varepsilon})_i^2 d\Omega}, \tag{14}$$

$$\eta^* = \sqrt{\frac{\|e_\varepsilon\|^2}{\|\varepsilon^*\|^2 + \|e_\varepsilon\|^2}}. \tag{15}$$

where m is the total number of elements. If the maximum permissible relative error $\eta^*_{\max}$ is given, we can define the maximum permissible error in any element i as

$$\|e_\varepsilon\|_{i,\max} = \frac{\eta^*_{\max}}{\sqrt{m}} \left(\|\varepsilon^*\|^2 + \|e_\varepsilon\|^2\right)^{1/2}. \tag{16}$$

In this research, the relative error η^* was calculated at each incremental step and remeshing began when η^* reached $\eta^*_{\max}$. The adaptive refinement takes effect around elements with errors larger than $\|e_\varepsilon\|_{i,\max}$. The larger $\eta^*_{\max}$ becomes, the narrower the refined area becomes.

To identify the refined region based on the candidate element for refinement, we propose a refining circle (Fig. 4), which consists of a center, the centroid of the candidate element for refinement and the radius (average diameter of three bubbles). In other words, the bubble to be placed within this refining circle will have a new bubble size in the next automatic mesh generation. The radius of a bubble in the refining circle is computed by

$$r_{new} = \left(\frac{\|e_\varepsilon\|_{i,\max}}{\|e_\varepsilon\|_i}\right)^q r_{ave}, \tag{17}$$

where r_{ave} is the average radius of three vertexes and q is the factor that controls the radius of a new bubble, r_{new}. The standard value of q is 1 and it is chosen as the user wants. If q is larger than 1, then the reduction ratio of bubble size becomes larger and smaller meshes are generated.

3.3 Transfer of data

When the regeneration of new mesh is completed, the data (boundary condition, loading condition, state variables, etc.) should be precisely transferred to search for the equilibrium position in the next incremental loading step. The information at the boundary node is particularly important in this algorithm, because the automatic mesh generation is started at the boundary nodes and new nodes may be inserted at the boundary lines for two cases in the remeshing stage. One is that a new node is inserted at the middle of the boundary line when the candidate element for refinement is adjacent to the boundary line. The other is that new nodes are inserted during boundary line packing of bubbles, when the distance between two nodes is greater than the sum of two bubble diameters due to the large deformation.

In the case when a new node is inserted at the boundary line, the boundary and contact conditions of the new node follow those of the nodes at both ends of the corresponding boundary line. State variables, such as strain and damage, are calculated at Gauss points and transferred in three steps:

[1] Transformation of Gauss point values into nodal point values in the old mesh by SPR

[2] Mapping between nodal point values in the old and new meshes

: Search of an old element to which a new node belongs + Interpolation of old nodal point value using the area coordinate

[3] Transformation of the nodal point values into Gauss point values in the new mesh

: Use of an average of three nodal point values owing to the 1-point Gauss quadrature rule

The nodal point values, such as displacement, are transferred in step 2.

4 Numerical Examples

Using the above algorithms, we analyzed the metal forming problems, such as upsetting and extrusion, to simulate the damage localization.

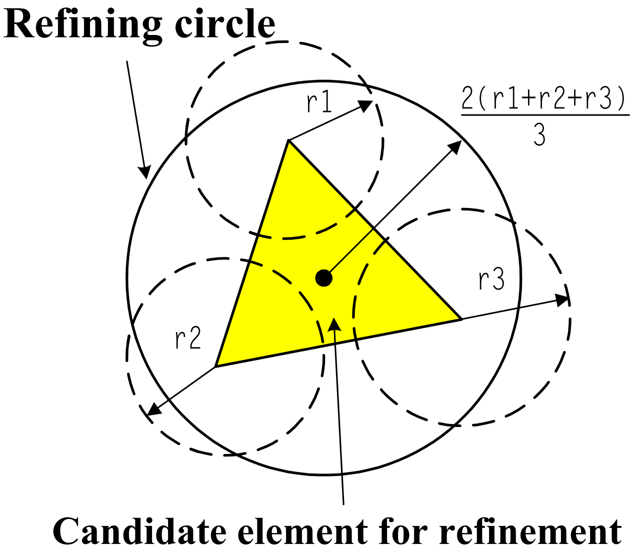

Figure 4 : Refining circle

4.1 Upsetting

A cross-section of the billet under die compression is shown as a numerical model in Fig. 5. For this research, only this cross-section, with a 16mm radius and 40mm height, was considered, using axisymmetry.

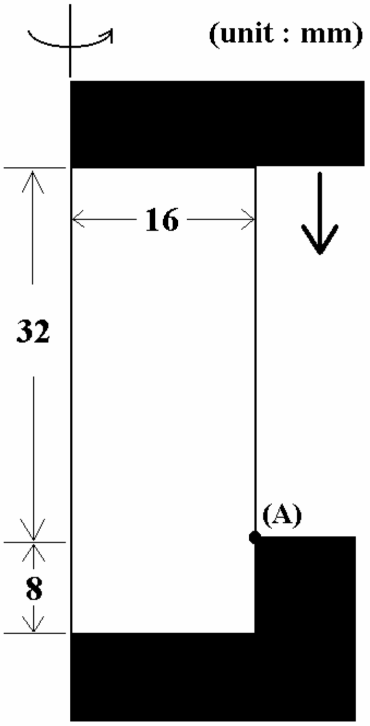

Figure 5 : Boundary and loading conditions of upsetting

First, we tested Mesh-1 and Mesh-2 without using adaptive refinement. The meshes were generated with uniform bubble sizes of 4mm(Mesh-1) and 1mm(Mesh-2) using BPM. The number of elements in Mesh-1 and Mesh-2 are 100 and 1512 respectively. Fig. 6 and Fig. 7 show the shapes and damage distribution of the meshes as the height of the billet is reduced for Mesh-1. The amount of distorted meshes increases as the reduction progresses. Especially, we could not produce a realistic deformation corresponding with the die shape around point (A). It can be seen that the damage distribution is uneven and it is difficult to express the concentrated damage using coarse meshes. The deformed shapes and damage distribution of Mesh-2 are shown in Fig. 8 and Fig. 9. The damage concentration in Mesh-2 can be seen more clearly than that in Mesh-1, but the distorted mesh still remains around point (A). These distorted meshes cause relative errors to increase as the billet height is reduced.

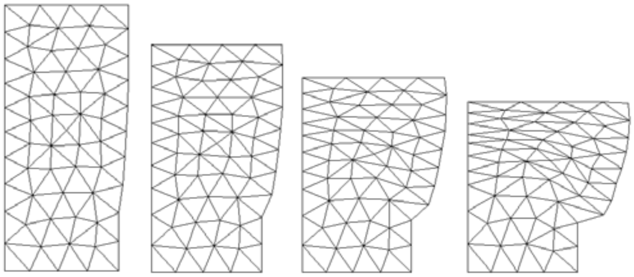

(a) 12.5% (b) 25% (c) 37.5% (d) 50%

Figure 6 : Deformed shapes of Mesh-1

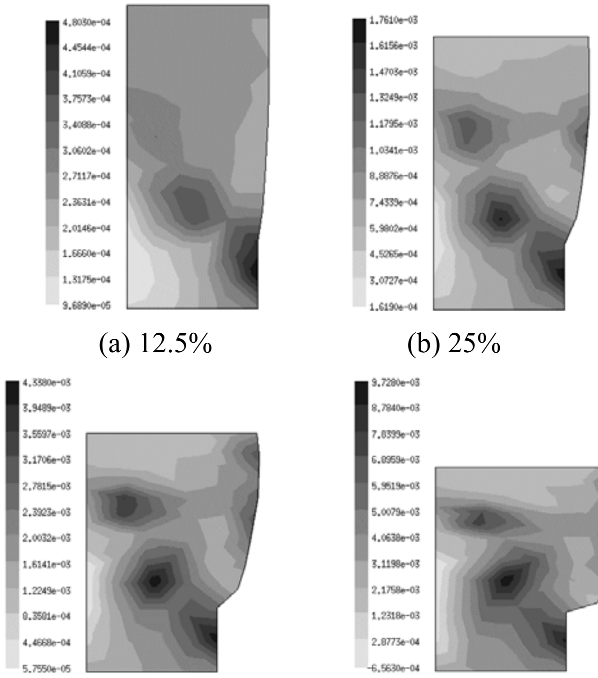

(a) 12.5% (b) 25%

(c) 37.5% (d) 50%

Figure 7 : Damage distribution of Mesh-1

Next, we tested Mesh-1 using adaptive refinement. $\eta^*_{\max} = 7.5\%$and $q = 1$ were adopted as the refinement criterion, and the error in equivalent strain is considered. The remeshing process was carried out three times and the meshes before and after remeshing and the error distribution before remeshing are displayed in Fig.10. The mesh quality defined by equation (18) was calculated and the averages of mesh qualities are also shown in Fig.10.

$$Q = 2\frac{r}{R} \tag{18}$$

where r is the radius of the inscribed circle and R is the radius of the circumscribed circle. Finer and regular triangle meshes were substituted for the meshes with large errors. Damage distributions in accordance with height reduction are shown in Fig. 11, in which we can clearly see the localized damage around point (A).

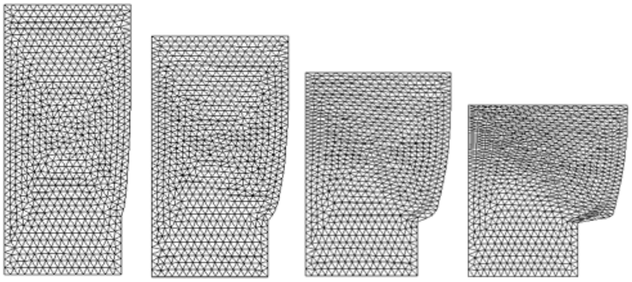

(a) 12.5% (b) 25% (c) 37.5% (d) 50%

Figure 8 : Deformed shapes of Mesh-2

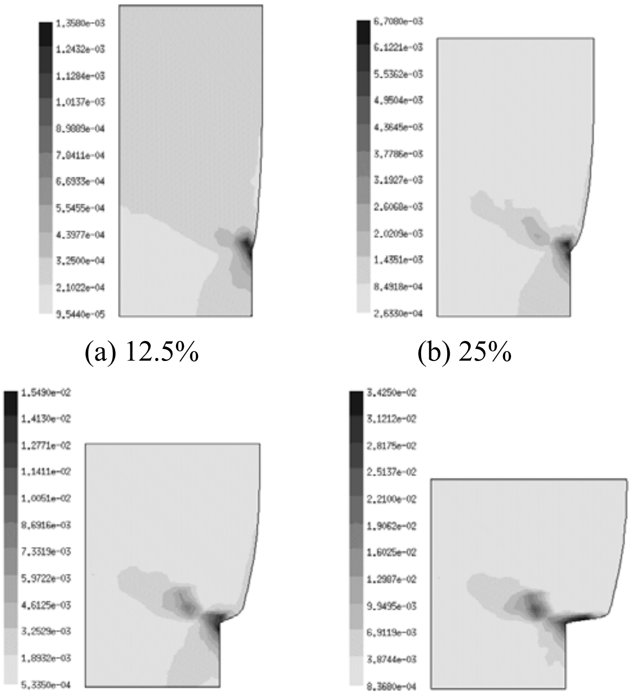

(a) 12.5% (b) 25%

(c) 37.5% (d) 50%

Figure 9 : Damage distribution of Mesh-2

Finally, we tested adaptive refinement again based on the error using damage variable ($e_d = d^* - \hat{d}$) instead of the equivalent strain to make sure that the damage localization was better simulated by the damage variable error. $\eta^*_{\max} = 24\%$ and $q = 1$ were used as the refinement criterion because the damage error was globally larger than the strain error. Remeshing was completed three times and the averages of mesh qualities are shown in Fig. 12. The error distribution shown in Fig. 12 is similar to that in Fig. 10 since damage increases where strain increases.

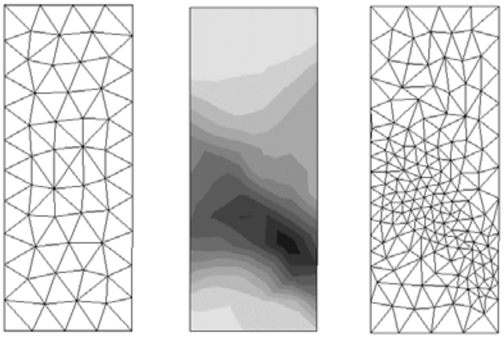

(a) 1st remeshing (1.6% height reduction)

Number of elements after remeshing : 322, $Q_{ave} = 0.876$

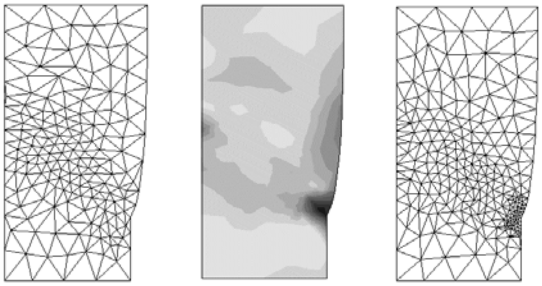

(b) 2nd remeshing (19% height reduction)

Number of elements after remeshing : 467, $Q_{ave} = 0.865$

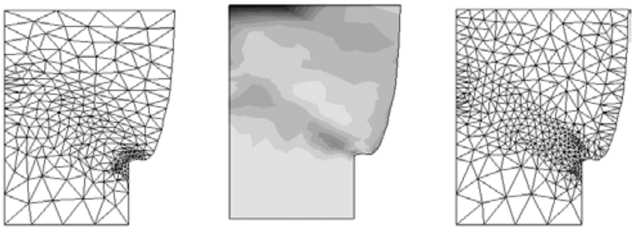

(c) 3rd remeshing (42.5% height reduction)

Number of elements after remeshing : 691, $Q_{ave} = 0.842$

Figure 10 : Finite element meshes before and after remeshing ($\eta^*_{\max} = 7.5\%, q = 1$) in upsetting (left : before remeshing, middle : error distribution, right : after remeshing)

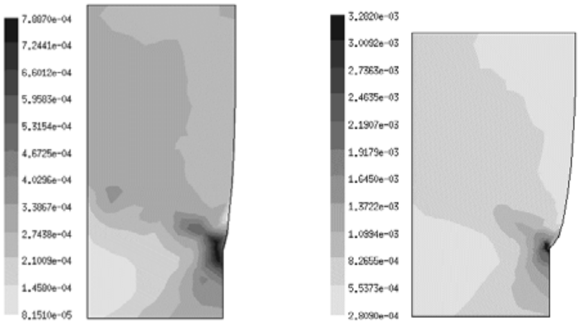

(a) 13.6% (b) 25.2%

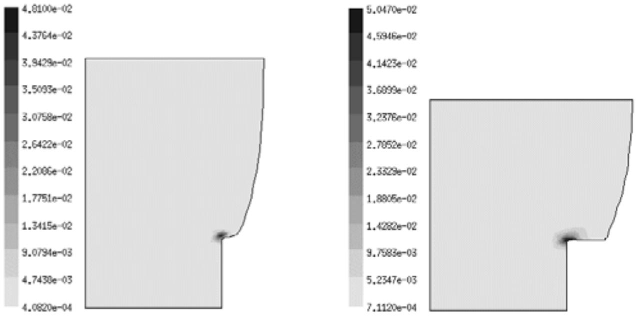

(c) 37.1% (d) 50.7%

Figure 11 : Damage distribution for remeshing with $\eta^*_{\max} = 7.5\%, q = 1$ in upsetting

The damage distributions are shown in Fig. 13, and we can clearly observe the damage localization at point (A). However, the increase of damage is slower in comparison with when a strain error is used because the refined meshes are generated directly in the regions with large damage gradients.

The predicted relative errors (η^*) for four cases are shown in Fig. 14. In the cases of Mesh-1 and Mesh-2, the errors increase monotonically as the height reduction increases. However, in the case with remeshing, as η^* reaches $\eta^*_{\max}$ and remeshing begins, the error decreases. Therefore, it can be concluded that adaptive refinement decreases error and clarifies damage localization.

4.2 *Extrusion*

The second example is an extrusion problem. The symmetric upper half of the specimen and die shapes are shown in Fig.15.

A uniform mesh (Mesh-3) with a bubble size of 5mm was generated and utilized in the analysis without remeshing. There were 1,112 elements and the deformed shapes are shown in Fig. 16. The wrinkle that appeared around point (B) during the initial compression loading still remains during a subsequent extrusion process. The mesh touching the corner of the die becomes more distorted

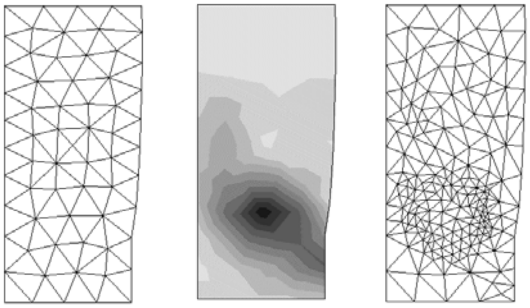

(a) 1st remeshing (12.3% height reduction)

Number of elements after remeshing : 338, $Q_{ave} = 0.847$

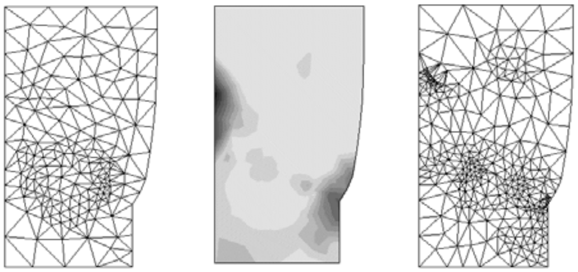

(b) 2nd remeshing (26.3% height reduction)

Number of elements after remeshing : 626, $Q_{ave} = 0.824$

(c) 3rd remeshing (43.3% height reduction)

Number of elements after remeshing : 803, $Q_{ave} = 0.823$

Figure 12 : Finite element meshes before and after remeshing ($\eta^*_{\max} = 24\%, q = 1$) in upsetting (left : before remeshing, middle : error distribution, right : after remeshing)

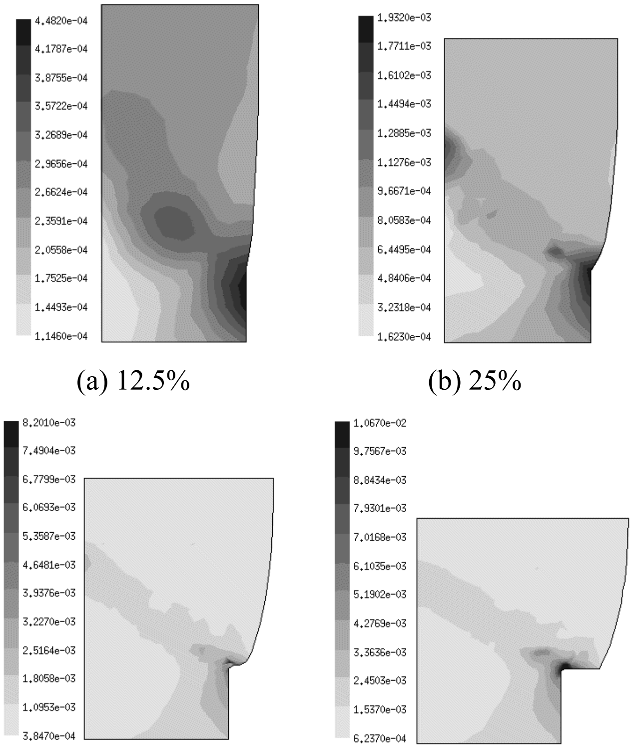

(a) 12.5% (b) 25%

(c) 37.5% (d) 50%

Figure 13 : Damage distribution for remeshing with $\eta^*_{\max} = 24\%, q = 1$ in upsetting

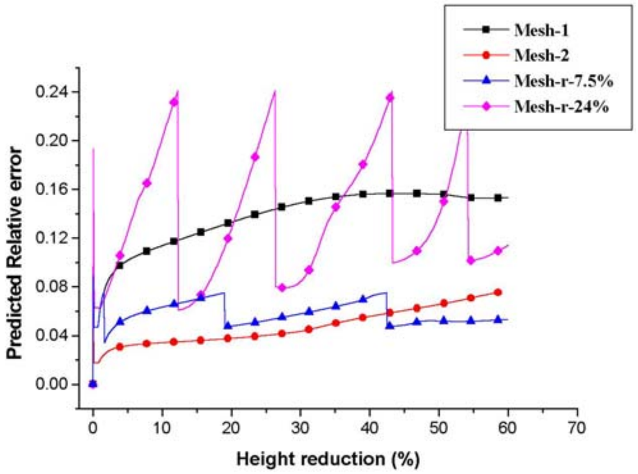

Figure 14 : Relative error vs. Height reduction

as the contact area becomes wider. The distributed damage variables are shown in Fig. 17. The damage around point (B) grows fast even during the initial compression loading and the regions touching the corners of the die become more damaged than any of the other regions.

In order to carry out adaptive refinement, we took a mesh with a bubble size of 10mm and 272 elements as the initial mesh. The equivalent strain error was calculated and the refinement criterion was $\eta^*_{\max} = 10\%$ and $q = 1$. Fig. 18 shows that the deformation was compatible with the geometry of the die and the distorted meshes were replaced with fine and regular triangle meshes during the four remeshing stages. When the initial mesh was used in the analysis without remeshing, we could not obtain the converged solution even at a 9% height reduction.

Localized damages around the contact area and point (B) are shown in Fig. 19. We established that damage localization could be simulated better by fewer elements if remeshing technique was used. Furthermore, the methodology used can be extended to the crack propagation problem [Zhang and Klein and Huang and Gao and Wu(2002), Cocchetti and Maier and Shen(2002)], that is to say, the mesh configuration will be redistributed along the new crack surface by the remeshing technique.

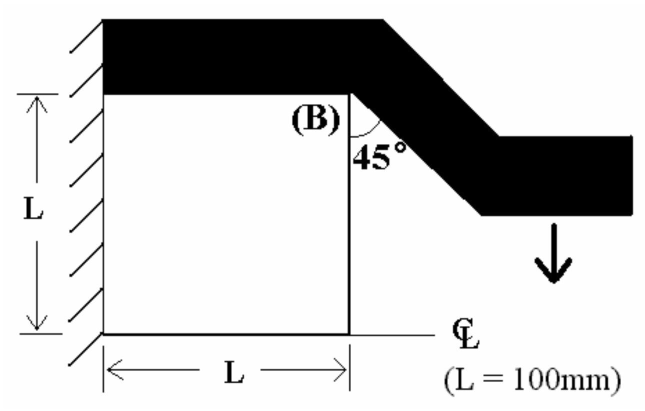

Figure 15 : Geometric description of extrusion

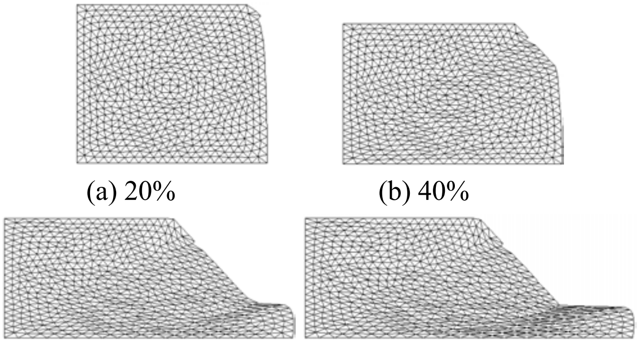
(a) 20%
(b) 40%
(c) 60%
(d) 64.6%

Figure 16 : Deformed shapes of Mesh-3 in extrusion

5 Conclusion

In this paper, the adaptive remeshing technique was applied for the simulation of localized damage based on the fact that the damage is concentrated at the severely deformed region. The developed adaptive refinement algorithm, based on the bubble packing method, utilized two parameters ($\eta^*_{\max}$, q) to easily acquire the refined mesh.

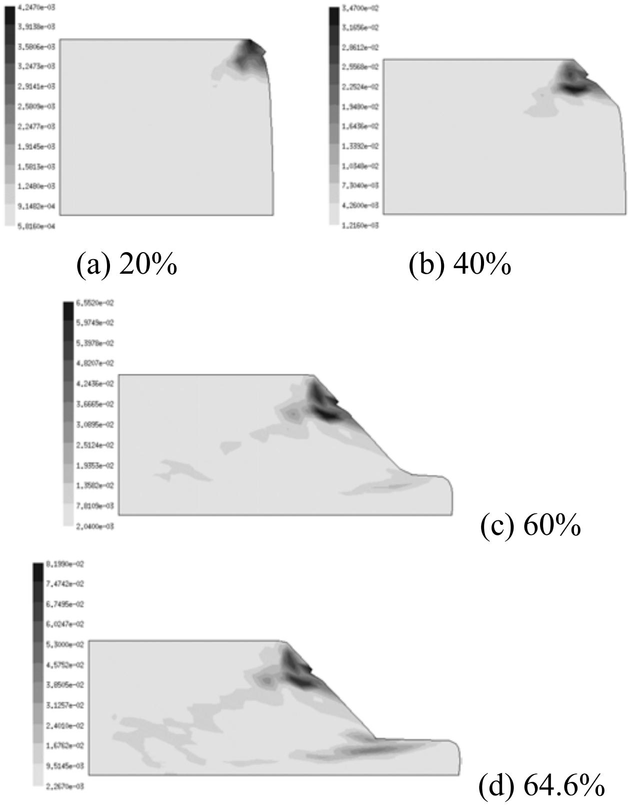
(a) 20%
(b) 40%
(c) 60%
(d) 64.6%

Figure 17 : Damage distribution of Mesh-3 in extrusion

Localized damage was monitored in the refined meshes for two metal forming problems. From the results, we can conclude that adaptive refinement has a beneficial effect on numerical simulations of localized damage and reduces error as well. Moreover, we can solve the problem of convergence arising from large deformations using a fewer amount of elements. We expect this research will extend usage of adaptive refinement through BPM to crack propagation and the strain localization studies in the near future.

Acknowledgement: We thank the Ministry of Science and Technology for the financial support given through the National Research Laboratory program. (Contract No. 00-N-NL-01-C-026)

References

Batra, R.C.; Ko, K.-I. (1992) : An adaptive mesh refinement technique for the analysis of shear bands in plane strain compression of a thermoviscoplastic solid, *Computational Mechanics*, Vol.10, pp.369-379.

(a) 1st remeshing (8.7% height reduction)

Number of elements after remeshing : 462, $Q_{ave} = 0.902$

(b) 2nd remeshing (14.6% height reduction)

Number of elements after remeshing : 499, $Q_{ave} = 0.882$

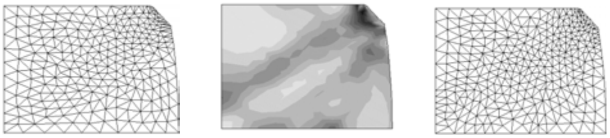

(c) 3rd remeshing (30.1% height reduction)

Number of elements after remeshing : 610, $Q_{ave} = 0.876$

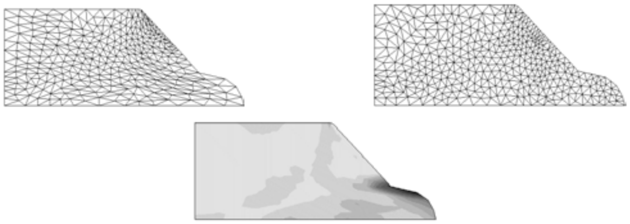

(d) 4th remeshing (60.8% height reduction)

Numbers of elements after remeshing : 737, $Q_{ave} = 0.869$

Figure 18 : Finite element meshes before and after remeshing ($\eta^*_{\max} = 10\%$, $q = 1$) in extrusion (left : before remeshing, middle : error distribution, right : after remeshing)

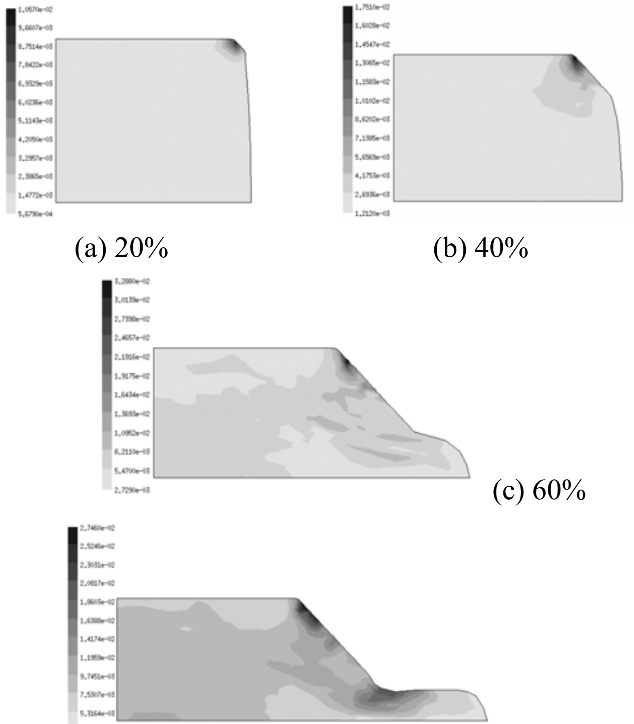

(a) 20% (b) 40%

(c) 60%

(d) 66.2%

Figure 19 : Damage distribution for remeshing with $\eta^*_{\max} = 10\%$, $q = 1$ in extrusion

Chen, Z.; Hu, W.; Chen E.P. (2000) : Simulation of dynamic failure evolution in brittle solids without using nonlocal terms in the strain-stress space, *CMES: Computer Modeling in Engineering & Sciences*, Vol.1, No.4, pp.57-62.

Cheng, Jung-Ho (1998) : Automatic adaptive remeshing for finite element simulation of forming process, *International Journal for Numerical Methods in Engineering*, Vol.26, pp.1-18.

Chung, Soon Wan; Kim, Seung Jo (2002) : A remeshing algorithm based on the bubble packing method and its application to large deformation problems", *Finite Elements in Analysis and Design*, Vol.39, No.4, pp.301-324.

Cocchetti, G.; Maier, G.; Shen, X.P. (2002) : Piecewise linear models for interfaces and mixed mode cohesive cracks, *CMES: Computer Modeling in Engineering & Sciences*, Vol.3, No.3, pp.279-298.

Du, Chongjiang (1998) : A note on finding nearest neighbors and constructing Delaunay triangulation in the plane, *Communications in Numerical Methods in Engineering*, Vol.14, pp.871-877.

Hatzigeorgiou, G.D.; Beskos, D.E. (2002) : Dynamic response of 3-D damaged solids and structures by BEM, *CMES: Computer Modeling in Engineering & Sciences*, Vol.3, No.6, pp.791-802.

Khoei, Amir R.; Lewis, Roland W. (1999) : Adaptive finite element remeshing in a large deformation analysis of metal powder forming, *International Journal for Numerical Methods in Engineering*, Vol.45, pp.801-820.

Kim, Jin Hee; Kim, Seung Jo; Kim, Wie Dae (1995) : A finite element analysis of damage propagation during metal forming process, *Engineering Fracture Mechanics*, Vol.51, No.6, pp.915-931.

Kim, Seung Jo; Chung, Soon Wan (1998) : Numerical simulation of finite rotation based on strain kinematics by polar decomposition, *International Conference on Computational Engineering and Science*, Atlanta, GA, October 6-9, pp.691-696.

Kim, Seung Jo; Kim, Jin Hee (1993) : Finite element analysis of laminated composites with contact constraint by extended interior penalty methods, *International Journal for Numerical Methods in Engineering*, Vol.36, pp.3421-3439.

Kim, S.J.; Kim, W.D.(1994) : A progressive damage modeling based on the continuum damage mechanics and its finite element analysis, ASME, *J. of Applied Mechanics*, Vol.61, pp.45-53.

Lee, C.K.; Hobbs, R.E. (1999) : Automatic adaptive finite element mesh generation over arbitrary two-dimensional domain using advancing front technique, *Computers & Structures*, Vol.71, pp.9-34.

Lemaitre, Jean (1996) : *A Course on Damage Mechanics*, Springer, pp.39-43.

Min, J.B.; Tworzydlo, W.W.; Xiques, K.E. (1995) : Adaptive finite element methods for continuum damage modeling, *Computers & Structures*, Vol.58, No.5, pp.887-900.

Mulmuley, Ketan (1994) : *Computational Geometry : An introduction through randomized algorithms*, Prentice-Hall, pp.288-299.

Ortiz, M.; Quigley, IV, J.J. (1991) : Adaptive mesh refinement in strain localization problems, *Computer Methods in Applied Mechanics and Engineering*, Vol.90, pp.781-804.

Paulino, G.H.; Menezes, I.F.M.; Neto, J.B. Cavalcante; Martha, L.F. (1999) : A methodology for adaptive finite element analysis : Towards an integrated computational environment, *Computational Mechanics*, Vol.23, pp.361-388.

PavanaChand, Ch.;KrishnaKumar, R.(1998): Remeshing issues in the finite element analysis of metal forming problems, *Journal of Materials Processing Technology*, Vol.75, pp.63-74.

Peerlings, R.H.J.; Borst R. de; Brekelmans, W.A.M.; Geers, M.G.D. (2002) : Localisation issues in local and nonlocal continuum approaches to fracture, *European Journal of Mechanics A/Solids*, Vol.21, pp.175-189.

Petersen, S.B.; Rodrigues, J.M.C.; Martins, P.A.F. (2000) : Automatic generation of quadrilateral meshes for the finite element analysis of metal forming processes, *Finite Elements in Analysis and Design*, Vol.35, pp.157-168.

Potyondy, David O.; Wawrzynek, Paul A.; Ingraffea, Anthony R. (1995) : An algorithm to generate quadrilateral or triangular element surface meshes in arbitrary domains with applications to crack propagation, *International Journal for Numerical Methods in Engineering*, Vol.38, pp.2677-2701.

Shimada, Kenji; Gossard, David C. (1998) : Automatic triangular mesh generation of trimmed parametric surfaces for finite element analysis, *Computer Aided Geometric Design*, Vol.15, pp.199-222.

Svedberg, Thomas; Runesson, Kenneth (2000) : An adaptive finite element algorithm for gradient theory of plasticity with coupling to damage, *International Journal of Solids and Structures*, Vol.37, pp.7481-7499.

Tradegard, A.; Nilsson, F.; Ostlund, S. (1998) : FEM-remeshing technique applied to crack growth problems, *Computer Methods in Applied Mechanics and Engineering*, Vol.60, pp.115-131.

Var Jr., M.; Owen, D.R.J. (2001) : Aspects of ductile fracture and adaptive mesh refinement in damaged elasto-plastic materials, *International Journal for Numerical Methods in Engineering*, Vol.50, pp.29-54.

Yang, Henry T.Y.; Heinstein Martin; Shih, J.M. (1989) : Adaptive 2D finite element simulation of metal forming processes, *International Journal for Numerical Methods in Engineering*, Vol.28, pp.1409-1428.

Zhang, P.; Klein, P.; Huang, Y.; Gao, H.; Wu, P.D. (2002) : Numerical simulation of cohesive fracture by the virtual-internal-bond model, *CMES: Computer Modeling in Engineering & Science*s, Vol.3, No.2, pp.263-278.

Zienkiewicz, O.C.; Zhu, J.Z. (1987) : A simple error estimator and adaptive procedure for practical engineering analysis, *International Journal for Numerical Methods in Engineering*, Vol.24, pp.337-357.

Zienkiewicz, O.C.; Zhu, J.Z. (1992) : The superconvergent patch recovery and a posteriori error estimates. Part 1 : the recovery technique, *International Journal for Numerical Methods in Engineering*, Vol.33, 1992, pp.1331-1364.